

# Accelerated Ripening in Chemically Fueled Emulsions\*\*

Marta Tena-Solsona<sup>+, [a, b]</sup> Jacqueline Janssen<sup>+, [c, d]</sup> Caren Wanzke,<sup>[a]</sup> Fabian Schnitter,<sup>[a]</sup> Hansol Park,<sup>[e]</sup> Benedikt Rieß,<sup>[a]</sup> Julianne M. Gibbs,<sup>[e]</sup> Christoph A. Weber,<sup>\*, [c, d]</sup> and Job Boekhoven<sup>\*, [a, b]</sup>

Chemically fueled emulsions are solutions with droplets made of phase-separated molecules that are activated and deactivated by a chemical reaction cycle. These emulsions play a crucial role in biology as a class of membrane-less organelles. Moreover, theoretical studies show that droplets in these emulsions can evolve to the same size or spontaneously self-divide when fuel is abundant. All of these exciting properties, *i. e.*, emergence, decay, collective behavior, and self-division, are pivotal to the functioning of life. However, these theoretical

predictions lack experimental systems to test them quantitatively. Here, we describe the synthesis of synthetic emulsions formed by a fuel-driven chemical cycle, and we find a surprising new behavior, *i. e.*, the dynamics of droplet growth is regulated by the kinetics of the fuel-driven reaction cycle. Consequently, the average volume of these droplets grows orders of magnitude faster compared to Ostwald ripening. Combining experiments and theory, we elucidate the underlying mechanism.

## 1. Introduction

Droplets are crucial for the spatial and temporal organization of the biochemistry in living cells.<sup>[1]</sup> These droplets, referred to as membrane-less organelles, can compartmentalize chemical reactions,<sup>[2,3]</sup> store genetic material,<sup>[4]</sup> and protect proteins from misfolding in response to environmental stress.<sup>[5]</sup> Chemical cues within the cell actively control the formation and properties of these droplets.<sup>[6,7]</sup> For example, the process of activation of the

main constituent proteins of P-granules<sup>[8]</sup> or stress granules<sup>[5]</sup> involves a chemical reaction cycle fueled by the hydrolysis of ATP.<sup>[9]</sup> Theoretical studies have shown that droplets in such chemically fueled emulsions can exhibit a set of different properties compared to emulsions approaching thermal equilibrium. For example, the droplet size within these emulsions can be regulated by the kinetics of the chemical reactions.<sup>[10,11]</sup> Similarly, the droplet position and the position of particles within the droplets can be controlled.<sup>[12,13,14]</sup> Finally, theoretical studies have shown that the droplets in these emulsions can spontaneously divide.<sup>[15,16]</sup> However, these theoretical predictions lack experimental systems to test them quantitatively. Examples of synthetic molecular assemblies regulated by fuel-driven reaction cycles have been described, including chemically<sup>[17–25]</sup> and photo-chemically fueled fibers,<sup>[17,18,23,26]</sup> dynamic vesicles formed by the consumption of ATP,<sup>[27]</sup> dynamic DNA-based assemblies,<sup>[28]</sup> colloids<sup>[29–32]</sup> and others.<sup>[33,34]</sup> Indeed, such studies result in surprising behavior like dynamic instabilities in synthetic fibers<sup>[19]</sup> or solutions of nanostructures that oscillate between different colors.<sup>[35]</sup> However, the field of chemically fueled droplets and emulsions remains mostly unexplored from an experimental perspective.<sup>[36,37]</sup> Experimental systems of these emulsions could validate theoretical predictions, demonstrate new physical and chemical behavior, and offer valuable insights into the mechanisms relevant for the regulation of membrane-less organelles.

In this work, we have developed synthetic, chemically-fueled emulsions (Figure 1a). The droplets in these emulsions emerge when chemical fuel is supplied, and they decay when all fuel is depleted. These emulsions show another surprising behavior, *i. e.*, the average volume of droplets in the emulsion increases rapidly. Moreover, we find that the rate of this growth is determined by the kinetic rates of the reaction cycle. The droplet growth shows similarities to Ostwald ripening but is up to two orders of magnitude faster. Similar to Ostwald ripening the average volume of the droplets is a result of the growth of large droplets at the expense of small ones (Figure 1b). By the

[a] Dr. M. Tena-Solsona,<sup>+</sup> Dr. C. Wanzke, F. Schnitter, Dr. B. Rieß, Prof. Dr. J. Boekhoven  
Department of Chemistry  
Technical University of Munich  
Lichtenbergstrasse 4, 85748 Garching (Germany)  
E-mail: job.boekhoven@tum.de

[b] Dr. M. Tena-Solsona,<sup>+</sup> Prof. Dr. J. Boekhoven  
Institute for Advanced Study  
Technical University of Munich  
Lichtenbergstrasse 2a, 85748 Garching (Germany)


[c] J. Janssen,<sup>+</sup> Dr. C. A. Weber  
Max Planck Institute for the Physics of Complex Systems  
Nöthnitzer Strasse 38, 01187 Dresden (Germany)  
E-mail: weber@pks.mpg.de


[d] J. Janssen,<sup>+</sup> Dr. C. A. Weber  
Center for Systems Biology Dresden  
Pfotenhauerstrasse 108  
01307 Dresden (Germany)


[e] H. Park, Prof. Dr. J. M. Gibbs  
Department of Chemistry, University of Alberta  
11227 Saskatchewan Drive  
T6G 2G2, Edmonton (Canada)

[<sup>+</sup>] These authors contributed equally to this work.

[\*\*] A previous version of this manuscript has been deposited on a preprint server (DOI: 10.26434/chemrxiv.9978539).

 Supporting information for this article is available on the WWW under <https://doi.org/10.1002/syst.202000034>

 An invited contribution to a Special Collection on Protocells and Prebiotic Systems.

 © 2020 The Authors. Published by Wiley-VCH GmbH. This is an open access article under the terms of the Creative Commons Attribution License, which permits use, distribution and reproduction in any medium, provided the original work is properly cited.

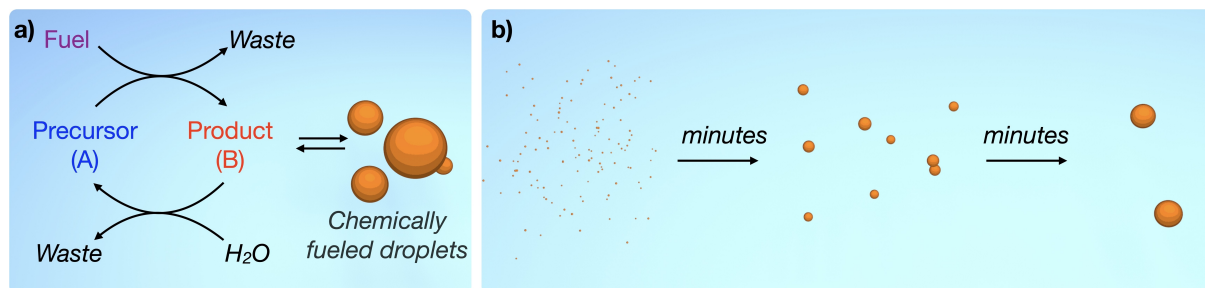


**Figure 1.** Schematic representation of fuel-driven droplet formation. a) A chemical reaction cycle drives the transition from the precursor (A) to the droplet-forming product (B) at the expense of a chemical fuel (activation). The droplet-forming molecules are unstable and will hydrolyze to the precursor (deactivation). b) Schematic representation of the experimentally observed droplet growth of the emulsion. Within minutes, many small droplets ripen to a few large ones.

quantitative agreement between experiments and theory, we propose a mechanism where the fuel-driven chemical reaction cycle can accelerate the growth of the average droplet volume. The mechanism relies on small droplets dissolving due to deactivation of droplet material while big drops grow due to activation of droplet material. This mechanism could be relevant for the control of growth speed and size of membrane-less organelles in living cells and could represent a new strategy of controlling nano-structures out-of-equilibrium.

## 2. Results and Discussion

### 2.1. Design of the Reaction Cycle

All emulsions in this work follow the same experimental design (Figure 1), *i.e.*, a water-soluble precursor (A) molecule is activated by an irreversible reaction with a fuel.<sup>[38,39]</sup> The product of that reaction (B) is less soluble and phase-separates into droplets. Moreover, this product B is intrinsically unstable and spontaneously deactivates via hydrolysis, yielding the original precursor A. That means that the emergence and sustenance of the emulsion require fuel, while the phase-separated droplets will decay and vanish in the absence of fuel. Thus, these emulsions are maintained away from thermodynamic equilibrium and are referred to as chemically fueled emulsions.<sup>[9]</sup> Since the water-soluble fuel is required for the activation and water is required for the deactivation, the chemical reaction cycle will almost exclusively take place in the aqueous phase.<sup>[29]</sup>

We study four reaction cycles that are all driven by the hydrolysis of 1-ethyl-3-(3-dimethylaminopropyl)carbodiimide (EDC) as a carbodiimide-based fuel. In all activation reactions, a carboxylate-based precursor A is activated by reaction with EDC (fuel). The activated precursor subsequently reacts with a second nucleophile in order to form the phase-separating product (B). These nucleophiles are an intramolecular carboxylate to form a cyclic anhydride (Cycle 1 and Cycle 2), an intermolecular carboxylate to form the symmetric anhydride (Cycle 3) or NHS to form the NHS-ester (Cycle 4). The deactivation reaction of the metastable products occurs via the hydrolysis of the product. We chose these reaction cycles

because their hydrolysis rate constants range over two orders or magnitude (Figure 2a). The wide range of rate constants allow for an exploration of the effects of chemical rates on the behavior of an active emulsion.

### 2.2. Molecular Design of the Precursor

The chemical reaction cycles depicted in Figure 2a were used to form emulsions by the hydration of EDC (fuel, Figure 2b). The precursors in each of the reaction cycles (Figure 2c) follow a simple molecular design. One domain (depicted in black) consists of a linear or branched aliphatic tail that drives phase-separation. The second domain (in blue) is the reactive domain that comprises one or two carboxylate-groups that makes the precursor well soluble. The loss of the negatively charged carboxylate(s) upon the activation reaction (anhydride or NHS-ester formation) results in a decrease in solubility inducing the formation of the emulsion.

### 2.3. Reaction Kinetics with Droplets

For each of the seven precursors depicted in Figure 2c, we followed the evolution of the reaction cycle in response to a single batch of the fuel (EDC) by measuring the concentration of precursor, product, and fuel by HPLC (Figure 3a-b and Supplementary Figure 2). In all cases, we found that the concentration of the metastable product initially rises, but decays as the system was running out of fuel. We can thus define a growth- and a decay-regime for each of these experiments. In the growth regime, activation dominates, and the product concentration increases. In contrast, in the decay-regime, fuel is depleted, and deactivation dominates.

For each cycle, the concentration of droplet-forming molecules decayed linearly throughout the decay-regime when droplets were present (Figure 3b and Supplementary Figure 2). The linear decay is a result of the constant deactivation rate (hydrolysis), which is induced by a self-protection mechanism of the droplets.<sup>[36,39]</sup> Because the droplets do not contain water, the deactivation takes place on the product fraction that

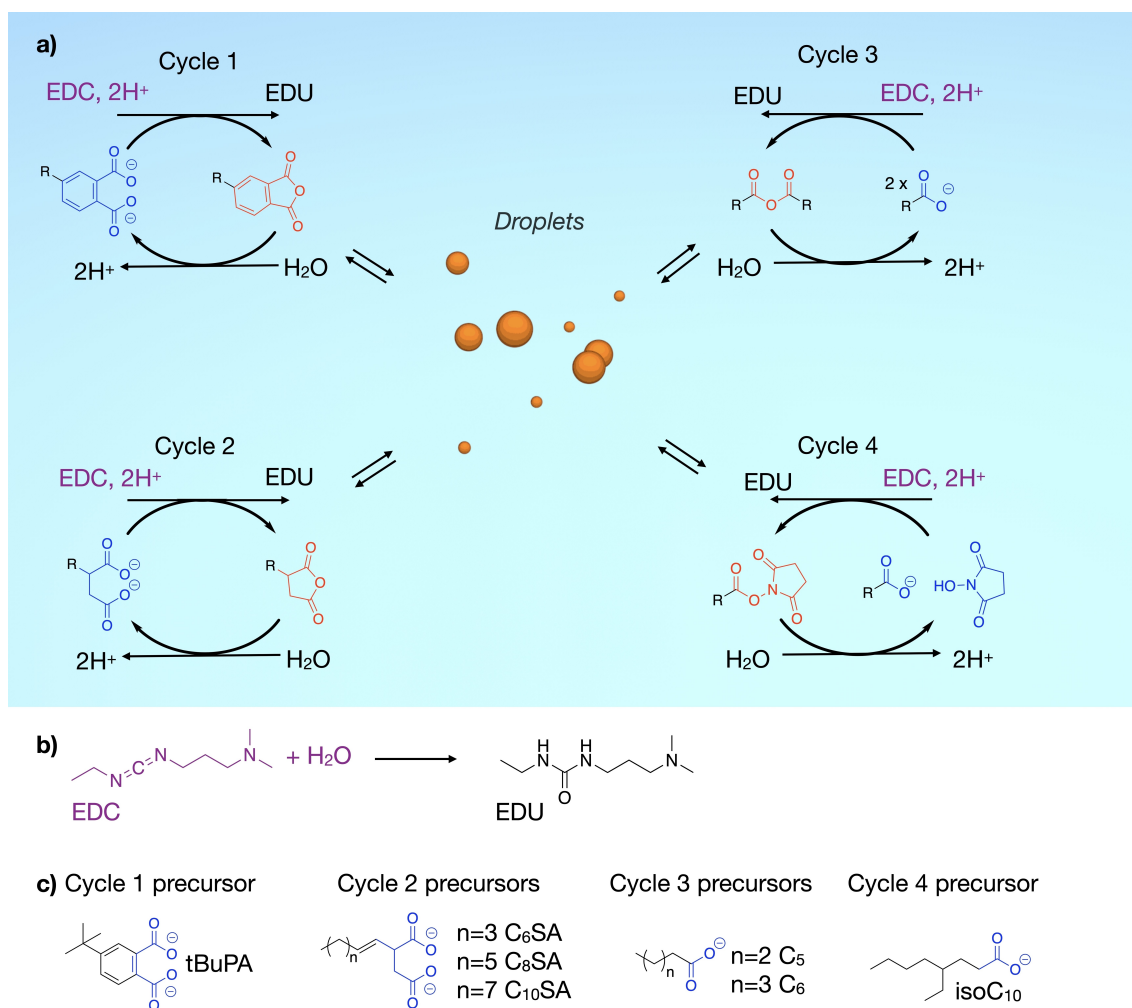


**Figure 2.** Chemical reaction cycles yielding emulsions. a) Four chemical reaction cycles that cause the formation of an emulsion. Each reaction cycle forms a hydrophobic product that phase-separates from water leading to oily, product-rich droplets. b) All reaction cycles are driven by the hydration of EDC. c) List of precursors used for each cycle.

remains in the aqueous phase (*i.e.*, outside of the droplets), which is close to the solubility ( $c_{\text{out}}^{(0)}$ ). The deactivation can thus be described by the effective rate:  $r_{\text{eff}} = k_d c_{\text{out}}^{(0)}$ . We determined the linear deactivation rate ( $r_{\text{eff}}$ ) and the solubility ( $c_{\text{out}}^{(0)}$ ) of all products (Supplementary Table 2). The linear decay of the product also implies that the precursor does not appreciably affect the kinetics of the hydrolysis reaction. The combined data allows calculating the deactivation rate constant ( $k_d$ ) of each of the products, which scale over two orders of magnitude from  $8.2 \cdot 10^{-3} \text{ s}^{-1}$  to  $4.9 \cdot 10^{-5}$  for cycle 1 to cycle 4, respectively (Supplementary Table 2).

#### 2.4. Rapid Growth of Average Droplet Size When Driven by a Single Batch of Fuel

By confocal microscopy and image analysis software, we measured the evolution of the droplet size in response to a single batch of fuel. To measure how the dynamics of the chemical reaction cycle affect the behavior of the droplets, we performed these experi-

ments on all products listed in Figure 2c, *i.e.*, the droplets formed by seven precursor-product combinations with vastly different reaction kinetics. It is worth mentioning that with a standard dynamic light scattering setup, we were not able to acquire reliable data due to the turbidity of the samples. For all droplet-forming reaction cycles, confocal microscopy showed that the droplets were present within the first minute after applying the fuel. The rapid formation of droplets points to a low nucleation energy and low capillary length which could be confirmed by theoretical estimates (Supplementary Section 4). Since the lateral resolution of the microscope is around 600 nm, the size of these initial droplets was likely overestimated. Indeed, a cryogenic transmission electron microscopy study showed that the droplets were below the resolution of the microscope (Figure S8). We thus discarded all data in the first minutes of the experiment and instead focused on the evolution of the droplet volume beyond the  $0.2 \mu\text{m}^3$ .

We found that for all products, the average volume of the droplets increased throughout most of the experiment. That included the growth-regime, but surprisingly, also the decay-regime in which the total product concentration was decreas-

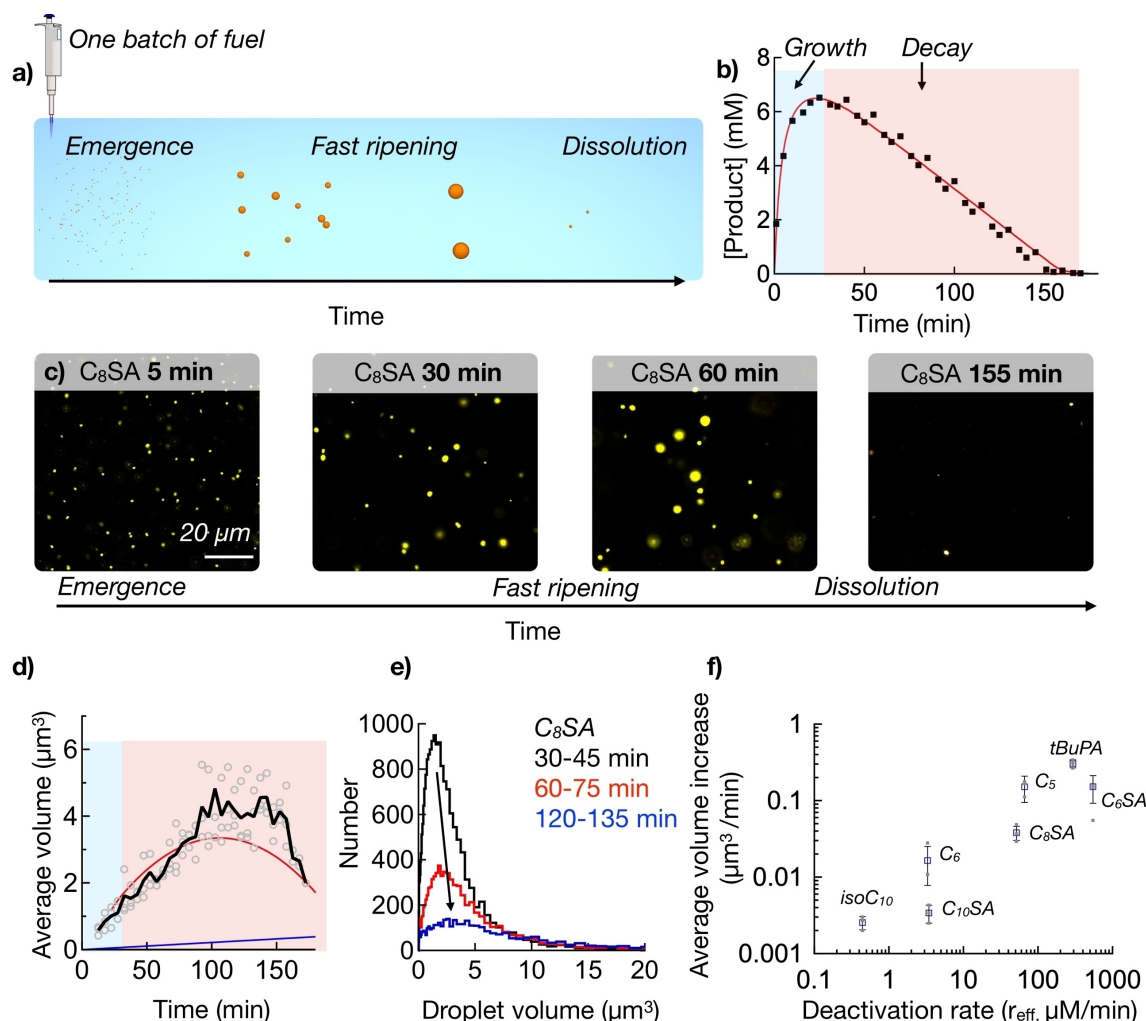


**Figure 3.** Behavior of batch-fueled emulsions. a) Schematic overview of the experiment: Droplets emerge, ripen, and dissolve in response to a batch of fuel. b) Total product concentration against time when 10 mM EDC is added to 10 mM  $C_8SA$ . Markers represent data measured by HPLC; the solid red line represents the calculated concentrations using our theoretical model. The growth- and decay-regime are shaded blue and red, respectively. c) Micrographs at several time-points in the cycle described in (b) as measured by image analysis software. The markers represent the data as measured by image analysis software in three experiments ( $n=3$ ), the black line represents the average of those three experiments. The solid red and blue lines represent calculated data for the accelerated ripening and Ostwald ripening, respectively. d) The average droplet volume against time for the system described in (b) as measured by image analysis software. The markers represent the data as measured by image analysis software in three experiments ( $n=3$ ), the black line represents the average of those three experiments. The solid red and blue lines represent calculated data for the accelerated ripening and Ostwald ripening, respectively. e) The distribution of droplet volume between 30–45 min, 60–75 min, and 120–135 min in the emulsions described in (b). f) Average volume growth rates against deactivation rates for all droplet-forming reaction cycles. The individual data points are shown (dots), their average (markers), and the standard deviation from the average (error bars,  $N=3$ ).

ing. For example, in the experiment with  $C_8SA$ , we found the average volume of the droplets increased for the first 140 minutes to almost  $5 \mu\text{m}^3$  (Figure 3c–d). After roughly 120 minutes, the droplet volume rapidly decreased, and the droplets disappeared (Figure 3d).

Interestingly, we found that the higher the deactivation rate, the greater the growth rate of the average droplet volume (Figure 3f, and Supplementary Table 2). For example, 4-tert-butylphthalic anhydride was one of the fastest deactivating products and the average volume of the droplets in the emulsion was the fastest increasing (Supplementary Figure 3). In contrast, the average volume of droplets in an emulsion of one of the slowest hydrolyzing products,  $C_{10}SA$ , increased slowly. The trend of increasing average droplet growth rate

with an increasing deactivation rate was observed for hydrolysis rates ranging over three orders of magnitude.

The histograms of the droplet population at different times in the cycle provided clarity on the increase in the average droplet volume (Figure 3e and SI4). The histograms show that, in the decay regime, the population of small droplets (e.g., below  $8 \mu\text{m}^3$ ) decreases rapidly. In contrast, the population of large droplets stays relatively constant. Consequently, the average droplet volume increases. However, this increase does not occur due to droplet growth, but because of the selective decay of small droplets. The loss of small droplets is particularly obvious when plotting the total number of droplets against time, which rapidly decayed (Supplementary Figure 3).

The behavior of average population growth at the expense of small droplets shows some reminiscence to Ostwald

ripening.<sup>[40]</sup> Ostwald ripening is a slow process that relies on diffusion of droplet molecules from small droplets to large ones driven by a shallow concentration difference among droplets. As a result, small droplets decay, while big ones grow (Figure 5b). While we observed the decay of small droplets, we did not find obvious growth of large ones in our experiments. Moreover, the average droplet volume growth was fast. To put that in perspective, we measured the growth rate of the average volume and compared them to theoretically calculated rates for classical Ostwald ripening<sup>[41]</sup> (Supplementary Table 3). We found that the growth rate of the average volume was faster compared to Ostwald ripening for all chemically fueled emulsions and the difference in growth rates between Ostwald ripening and the observed rate was more pronounced with increasing hydrolysis rate constant. For example, the growth rate for the slowest hydrolyzing emulsion (iso-C<sub>10</sub>) was a 1.2-fold faster compared to Ostwald ripening. In contrast, the growth rate for C<sub>6</sub>SA was 19 times faster than one would expect based on Ostwald ripening. The fastest-growing droplets were formed by 4-tert-butylphthalic anhydride, of which the average volume grew a 95-fold faster compared to Ostwald ripening.

### 2.5. Faster Average Droplet Volume Increase When Driven by a Pseudo-continuous Supply of Fuel

In the experiments above, a finite amount of fuel was initially added as a batch resulting in transient droplets of which the average volume rapidly increased. Such experiments contrast living systems where fuel levels are continuously maintained, and reaction cycles may reach a steady state, *i.e.*, activation equals deactivation.<sup>[42]</sup> We thus tested the droplets in a steady state, and we used a reaction-diffusion model to calculate the flux of fuel required to reach steady states (Supplementary equation (19) for an estimate). To avoid the need for stirring the sample, which affected droplet behavior, we applied a batch of fuel every few minutes and homogenized the sample by shaking it briefly (Figure 4a). We used HPLC to confirm the formation of such a steady state in the concentration fuel and product with pseudo-continuous fueling (Figure 4b and S4). We found that because of the pseudo-continuous fueling, the concentration product would fluctuate around steady state, but fluctuations were never greater than  $\pm 5\%$  of the concentration.

We found that the average droplet volume in the emulsions in a steady state also increased rapidly (Figure 4c–d). Moreover, the increase was faster compared to the droplets that were batch-fueled (Supplementary Table 3). For example, when C<sub>8</sub>SA was brought to steady state of roughly 7 mM, the average droplet volume increased almost three times faster compared to the batch-fueled experiments and more than 60 times faster compared to classical Ostwald ripening (Figure 4c–e, Supplementary Table 3). The rapid increase of the average volume was further confirmed for other emulsions in a steady state, like C<sub>6</sub>SA and C<sub>10</sub>SA (Figure 4c). Again, we found in these experiments that the average droplet volume growth scaled linearly with the deactivation rate of the reaction cycle (Figure 4f). For

C<sub>6</sub>SA, the rate was the highest, with almost  $0.6 \pm 0.2 \mu\text{m}^3/\text{min}$ . Such a growth rate means that droplets had reached an average volume of  $15 \mu\text{m}^3$  after a two-hour experiment. In contrast, the lower steady state dynamics of the C<sub>10</sub>SA droplets resulted in a much slower droplet growth.

The size distributions of the droplets as a function of time revealed that additional effects that were involved in the growth of droplets in steady state compared to those fueled with a single batch. In the batch-fueled experiments, small droplets were decaying faster compared to Ostwald ripening, but large droplets were not growing significantly (Figure 3e). In contrast, in the pseudo-continuously-fueled experiments, large droplets were growing while small droplets were decaying fast (see Figure 4e). The combination of the rapid growth of large droplets and fast decay of small ones further accelerated droplet growth compared to batch-fueled experiments.

### 2.6. Theoretical Model of Accelerated Ripening

To understand the mechanism of rapid droplet growth, we propose a theoretical model that describes phase separation with chemical reactions that can quantitatively describe how the reaction cycle affects the droplet behavior. Our model accounts for phase-separation between product and solvent, diffusion, and all chemical reactions between the fuel *F*, precursor *A*, and product *B* (see Supplementary Information for a full derivation and more details on the model). In our model, fuel (*F*) is added with a rate  $j_F$  and reacts with a rate proportional to fuel concentration  $c_F$  and precursor concentration  $c_A$  and a rate constant  $k_F$ . This reaction leads to the activation of the precursor to form product. The product is spontaneously deactivated with a rate  $k_d$  back to precursor. In addition, the product can diffuse with a diffusion coefficient  $D_B$  among the droplets allowing the droplets to exchange material and thereby undergo Ostwald ripening. In our model, droplets act as sources and sinks of product molecules with rate  $J$  and impose phase separation conditions at the droplets' interfaces (Gibbs-Thomson boundary condition). Thus, outside the droplets, the kinetics of the concentrations  $c_i$  ( $i = F, A, B$ ) is governed by [Eq. (1)]:

$$\partial_t c_F = -k_F c_F c_A + j_F \quad (1a)$$

$$\partial_t c_A = -\lambda k_F c_F c_A + k_d c_B \quad (1b)$$

$$\partial_t c_B = \lambda k_F c_F c_A - k_d c_B + D_B \nabla^2 c_B - J \quad (1c)$$

where  $\lambda$  denotes the yield factor. It reflects that not all fuel molecules actually lead to a product due to the metastability of the O-acylisourea intermediate compound (see Supplementary Eq. (5)). The rate  $J$  determines the total growth of drops, and thereby how the average volume changes with time. Numerical solutions to the model show a good agreement with the concentrations of fuel and total product concentration measured by HPLC (Figure 3b, and S2). For batch-fueled experiments ( $j_F = 0$ ), the model can quantitatively describe the fast initial

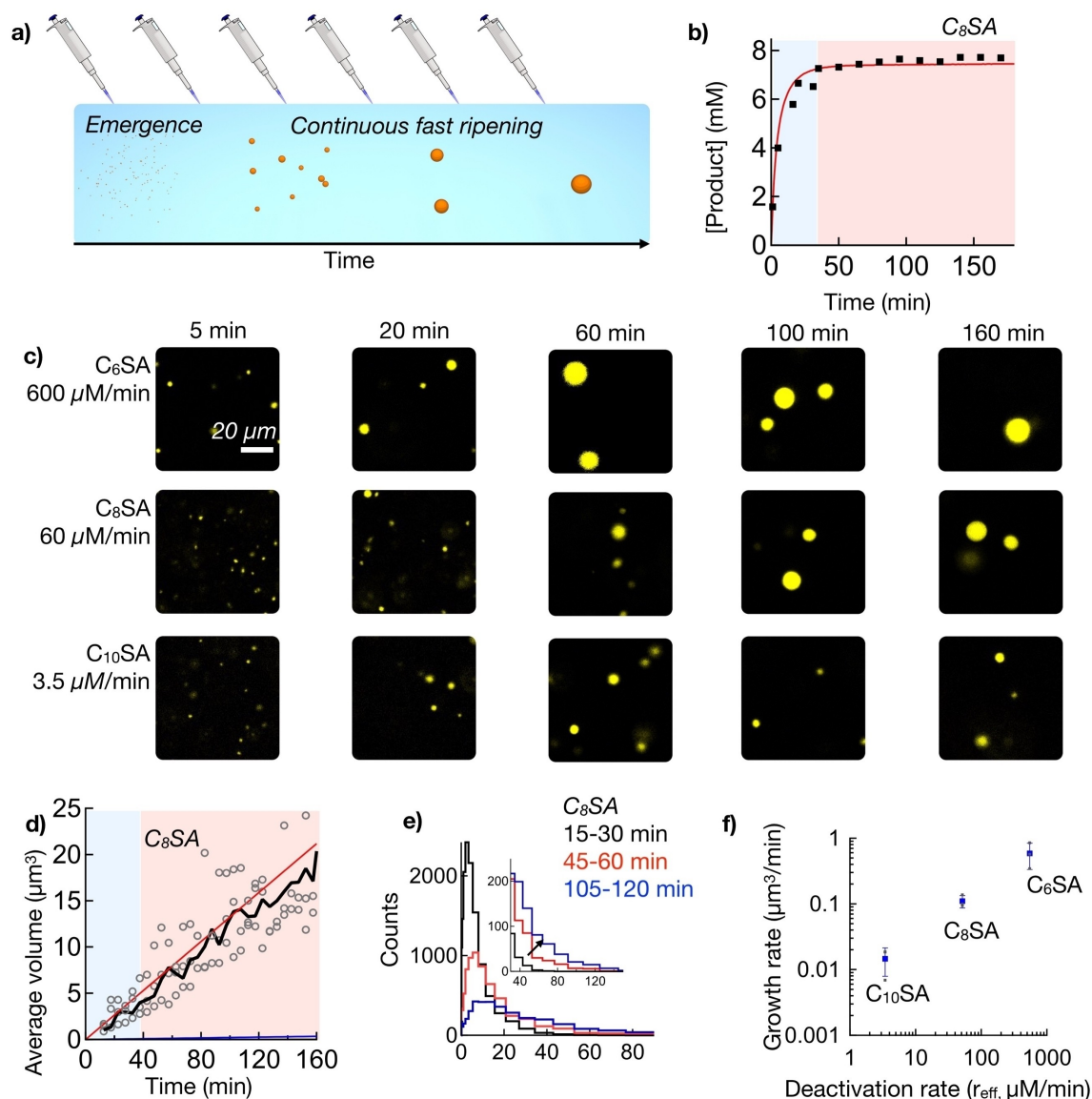


**Figure 4.** Behavior of pseudo-continuously fueled emulsions. a) Schematic overview of the experiment: droplets emerge and continuously ripen when pseudo continuously fueled by batches of fuel. b) Concentration profile of total product concentration measured by HPLC approaching a steady. Droplet formation was induced by an initial batch of fuel (10 mM EDC to 10 mM  $C_8$ ), and the system was maintained in steady-state by pseudo continuously fueling with 4 mM EDC/hr. Markers represent data measured by HPLC; the solid red line represents the calculated concentrations using our theoretical model. The growth- and steady-state-regime are shaded blue and red, respectively. c) Micrographs of droplets of  $C_6$ SA,  $C_8$ SA, and  $C_{10}$ SA in a steady-state by continuous addition of fuel. d) Average droplet volume over time for experiment discussed in (a). The markers represent the data as measured by image analysis software in three experiments ( $n=3$ ), the black line represents the average of those three experiments. The solid red and blue lines represent calculated data for the accelerated ripening and Ostwald ripening, respectively. e) The distribution of droplet volume at 30, 60, and 120 minutes of the emulsion described in (a). f) Average volume growth rates against the deactivation rate. The individual data points are shown (dots), their average (markers), and the standard deviation from the average (error bars,  $N=3$ ).

activation of the total product concentration up to its maximum at time  $t_{\max}$ , as well as the linear decrease with a slope equal to the effective deactivation rate  $r_{\text{eff}} = k_d c_{\text{out}}^{(0)}$  for times  $t > t_{\max}$ , where  $c_{\text{out}}^{(0)}$  is the solubility. Due to the good agreement of the model solutions with all experimental traces for total product, precursor and fuel concentrations corresponding to all reaction cycles and the various precursors, we use it to extract the rate constants of the reactions. These rate constants allow us to also quantitatively describe the pseudo-steady state experiments

(Figure 4b and S4). In addition, these rate constants are used to theoretically predict the growth of the average droplet volume.

From our model, we derived an approximate mathematical expression of how the average droplet volume changes with time,  $\langle V \rangle(t)$ , for both fueling protocols (Supplementary Equation (28, 29)) and valid for  $t > t_{\max}$ . This expression reads [Eq. (2)]:

$$\langle V \rangle(t) \simeq (m_{\text{clas}} + m_{\text{fueled}})t - \tilde{m} t^2 \quad (2)$$

where  $m_{\text{clas}}$  denotes the growth rate corresponding to Ostwald ripening which depends on the interfacial tension of the product rich-phase coexisting with solvent, the solubility of the product, product molecular volume and its diffusion constant. In separate experimental studies, we have determined those parameters for all considered chemical systems allowing us to estimate the relevance of Ostwald ripening for our fuel-driven systems (see Supplementary Table 2). The additional contributions arising from the fuel-driven chemical reaction cycle are  $m_{\text{fueled}}$  and  $\tilde{m}$ . Most importantly, our derivation gives explicit expression for contributions to the slope related to chemical fueling as a function effective deactivation rate  $r_{\text{eff}}$ . Specifically [Eq. (3)]:

$$m_{\text{fueled}} = \alpha \nu V_{\text{sys}} r_{\text{eff}} \quad (3)$$

where  $V_{\text{sys}}$  is the system size,  $\nu$  is the molecular volume of product and  $\alpha$  is a numerical prefactor which varies between the two fueling protocols but is the same for all reaction cycles (see Supplementary Eq. (29)). The remaining fuel related growth rate  $\tilde{m}$  is zero in the pseudo-continuously fueled mode, while for the one batch mode, it is determined by the amount of initially added fuel (see Supplementary Eq. (30)). Substituting the known parameter values related phase separation and the fuel-driven chemical reactions (see Supplementary Table 2) into Eq. (2,3), we find a good agreement the experimental measurements (red lines in Figure 3d, 4d, and Supplementary Figure 3 and 5).

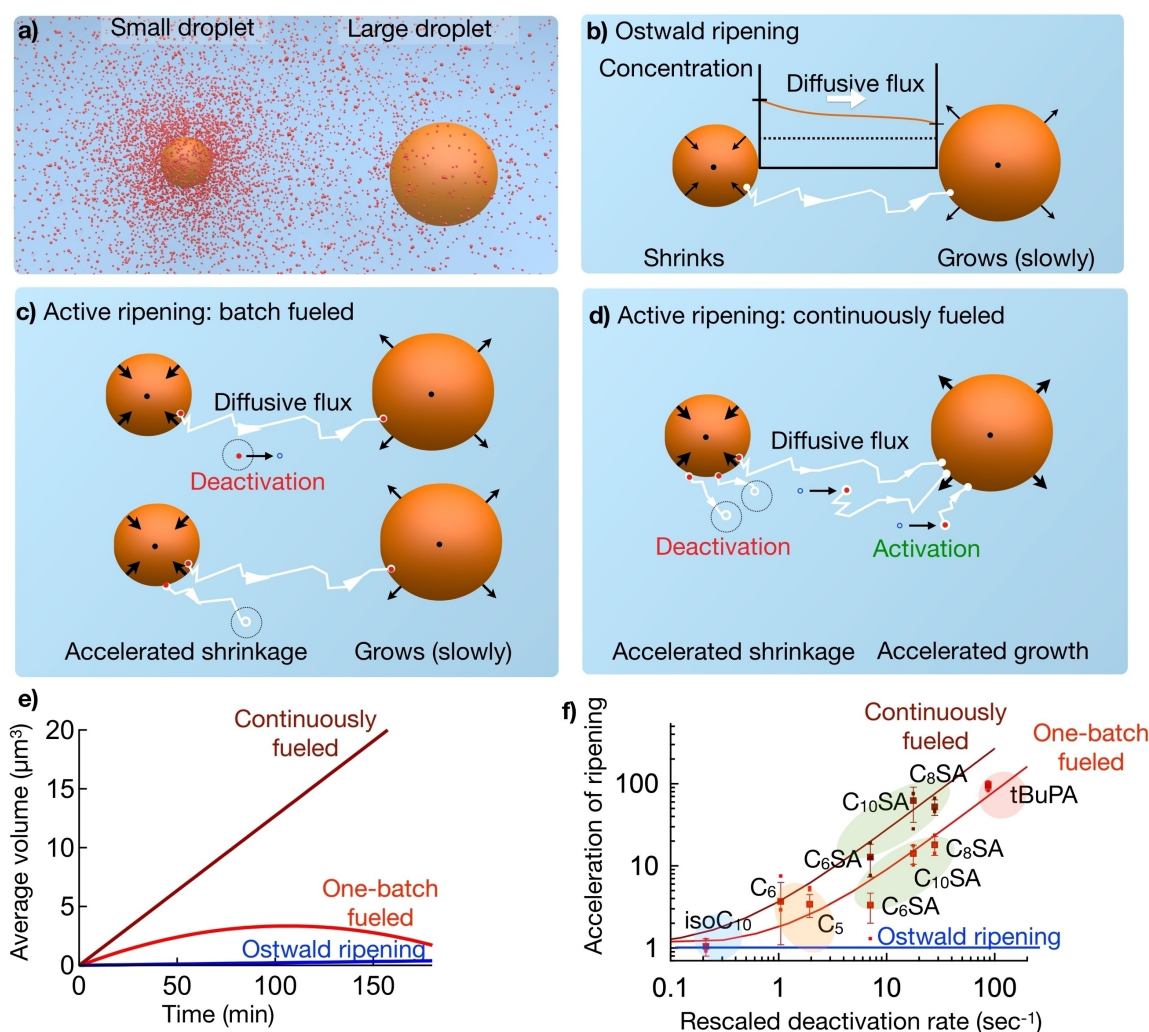


**Figure 5.** Mechanism of rapid droplet growth. a) Schematic representation of product molecules (red sphere) around a small droplet (left orange sphere) and large droplet (right orange sphere). Due to a different Laplace pressure, a small droplet is surrounded by a higher concentration of product than a large droplet. b) Due to the concentration gradient described in (a), molecules diffuse from small to large droplets. Consequently, the droplet population ripens, i.e., big droplets grow, while small drops decay. c) The deactivation reaction increases the efflux from small droplets. d) In the presence of fuel, the activation of the product leads to additional faster growth of large droplets compared to (c). e) Theoretically calculated average droplet volumes as a function of time for  $\text{C}_8\text{SA}$  subjected to Ostwald ripening (blue), accelerated ripening when fueled with a single batch (red), and accelerated ripening when fueled continuously (dark red). f) Acceleration of ripening against the rescaled deactivation rate when products are subjected to one batch of fuel (red) or when continuously fueled (dark-red). The products are grouped per reaction cycle (blue for cycle 4, orange for cycle 3, green for cycle 2, and red for cycle 1). The individual data points are shown (dots), their average (markers), and the standard deviation from the average (error bars, N=3).

## 2.7. Mechanism of Accelerated Ripening

The agreement between experiment and theory suggests that the mechanism underlying droplet growth in the model coincides with the one in the experiment, *i.e.*, the rapid ripening is based on a combination of Ostwald ripening and the fuel-driven reaction cycle. Ostwald ripening occurs because smaller droplets have a greater Laplace pressure compared to large droplets. This difference leads to a slightly higher concentration of droplet molecules around small droplets compared to large ones (Figure 5a). Consequently, a diffusive flux of the droplet molecules from small to big droplets is established that scales with the surface tension. This diffusive flux drives the slow growth of the bigger droplets at the expense of smaller shrinking ones, which eventually dissolve (Figure 5b). In our chemically-fueled emulsions, a similar concentration gradient emerges between small and big droplets (Figure 5c). However, besides the diffusive flux among droplets, the chemical kinetics of product activation and deactivation significantly alter the fluxes of product molecules in the system and thereby accelerates droplet ripening.

First, we describe how the deactivation of product molecules can accelerate the growth of the average droplet volume. The deactivation occurs in the aqueous phase of the emulsion (between the droplets) and can create a local undersaturation, *i.e.*, upon deactivation, the local concentration is slightly lowered below the solubility concentration of the product (Figure 5c). This local undersaturation is rapidly restored via diffusion of product molecules from one of the surrounding droplets. However, because of the concentration gradient between small and large droplets, the local undersaturation is more likely to be “filled” by products expelled from a small droplet. Deactivation thus selectively decreases the volume of small droplets compared to large droplets. That selective efflux from the small droplets results in an accelerated decay of small droplets compared to Ostwald ripening (Figure 3d). Moreover, this accelerated decay of the small droplet population leads to an increase of the average droplet volume that is faster compared to Ostwald ripening and is regulated by the kinetics of the deactivation: the faster the deactivation, the faster the ripening (Figure 3f). Finally, once droplet numbers are low and the droplets are on average far apart, diffusion can no more catch up with the deactivation reaction. Consequently, remaining droplets quickly dissolve, and the system becomes homogeneous, which we observed experimentally (Figure 3c–d).

In the case of pseudo-continuous fueling, both deactivation and activation affect the evolution of the droplets' size. Small droplets dissolve faster compared to Ostwald ripening because of the mechanism discussed above (Figure 5c). In addition, the activation reaction continuously activates product in the aqueous phase which is leading to a locally enhanced supersaturation (Figure 5d). This increase of supersaturation is more likely to be “absorbed” by a large droplet rather than by a small one because products diffuse down the concentration gradients created by the Laplace pressure differences among the droplets. The combined mechanism implies an accelerated decay of small droplets (*via* deactivation) and accelerated growth of

large droplets (*via* activation). Interestingly, the simultaneous occurrence of both phenomena is visible in the evolution of the histograms, *i.e.*, the population of small droplets vanishes, while the population of large droplets grows (Figure 4e).

An alternative mechanism for an increase of the average volume is fusion of droplets. However, in all experiments no droplet fusion was observed (Supplementary Figure S7). Sporadically, droplets collided and appeared stuck to one another, but they would eventually unstuck. Consistently, using theoretical estimates, fusion is shown to be too slow to contribute to the ripening rate for the chemical systems considered (Supplementary Figure S7). We also challenged the model assumption that activation and deactivation dominantly occur outside the droplets instead at the droplet interface. In particular, the concentration of product molecules at the droplet interface is rather high compared to the product concentration outside the droplets. However, the rate of hydrolysis events at a droplet interface is still negligible compared building blocks being hydrolyzed in the surrounding corresponding to a typical droplet (Supplementary Section 4).

Our proposed mechanism explains that the average volume of droplets in a chemically fueled emulsion increases faster compared to Ostwald ripening because droplet material is deactivated in the batch-fueled experiments, or both activated and deactivated in the continuously fueled experiments. The mechanism also explains the difference in ripening rates between the two fueling protocols, *i.e.*, ripening is fastest when continuously fueled (Figure 5e). Our theory suggests that a combination of parameters (activation and deactivation rates, solubility, surface tension, and molecular volume) determine the faster growth of the average volume compared to Ostwald ripening (Supplementary Equation (31)). We combine these parameters into a rescaled effective deactivation rate such that it represents a measure that determines the ripening rate compared to Ostwald ripening. We plot the degree of acceleration compared to Ostwald ripening, *i.e.*, the measured growth rates divided by the theoretical Ostwald ripening rates, as a function of this rescaled deactivation rate (Figure 5f), and find excellent agreement between experimental data and theory. From this plot, it becomes clear that the ripening of iso-C<sub>10</sub>, with the lowest rescaled deactivation rate, is almost exclusively driven by Ostwald ripening. In contrast, tBuPA is accelerated by almost two orders of magnitude compared to Ostwald ripening due to its large deactivation rate constant. Finally, the plot demonstrates that continuously fueled emulsions will ripen faster than batch-fueled emulsions by a factor of 2–5.

## 3. Conclusion

In this work, we described a new behavior in chemically fueled emulsions, *i.e.*, the increase of the average droplet volume is regulated by the kinetics of the underlying chemical reaction cycle. We designed four chemical reactions cycles with reaction rates that span over three orders of magnitude in order to quantitatively understand the behavior, and we find that the faster the reaction cycle, the greater the acceleration of average droplet volume. Given the simplicity of the mechanism, we anticipate that the behavior can be observed in other fuel-



driven assemblies. For example, accelerated growth could be observed in membrane-less organelles, provided that protein activation and deactivation occur outside of the organelle (e.g., by kinases that operate in the cytosol, but not in the organelle). The mechanism could thus help to explain how the growth of membrane-less organelles is regulated. Our theoretical model further validates the generality of the accelerated ripening. Moreover, we believe the mechanism will hold for crystal growth or the synthesis of nanoparticles, which are also subjected to Ostwald ripening. Such accelerated growth will be particularly powerful for the synthesis micro- and nanostructures of tunable size. For example, once an emulsion has reached a certain average droplet size via the accelerated ripening, the droplets can be polymerized.

## Methods

### Materials

4-Morpholineethanesulfonic acid (MES) buffer, pentanoic acid, hexanoic acid, 2-hexenyl-succinic anhydride, 2-octenyl-succinic anhydride, 2-decenyl-succinic anhydride, t-butyl-phthalic anhydride, 4-ethyloctanoic acid, 1-Ethyl-3-(3-dimethylaminopropyl) carbodiimide (EDC), N-hydroxysuccinimide (NHS) and Nile Red were all purchased from Sigma-Aldrich and Alfa-Aesar unless indicated otherwise. The precursors  $C_6SA$ ,  $C_8SA$ ,  $C_{10}SA$ , and  $isoC_{10}$  were synthesized by hydrolysis of their corresponding anhydrides. The anhydrides were suspended in demineralized water and hydrolyzed over 48 hours while stirring the samples. The absence of anhydride was assessed by HPLC. The samples were freeze-dried and stored at  $-20^\circ C$  until further use. Their purity was assessed by and Electro-spray Ionization-Mass Spectroscopy (ESI-MS) and HPLC.

### Sample Preparation

We prepared stock solutions of the precursors by dissolving it in MES buffer and subsequently adjusting the pH to 6.0. We used 200 mM of MES buffer for precursor concentrations of 10 mM or less. For higher precursor concentrations, we used a buffer concentration of 500 mM. We used the precursors at the following concentrations: 300 mM  $C_5$ , 100 mM  $C_6$ , 10 mM of  $C_6SA$ , 10 mM of  $C_8SA$ , 7.5 mM of  $C_{10}SA$ , 10 mM of tBuPA, and 5 mM of  $isoC_{10}$ . We prepared the stock solutions of EDC by dissolving the EDC powder in demineralized water, typically, at 1.0 M EDC. We initiated the batch-fueled experiments by the addition of various batch-sizes of EDC to the precursor solution. In the case of  $isoC_{10}$ , the addition of fuel was accompanied by the addition of 5 mM of NHS. We initiated the pseudo-continuously fueled experiments by the addition of an initial amount of EDC fuel. Specifically,

50 mM of EDC was added to 10 mM of  $C_6SA$ , 10 mM of EDC was added to 10 mM  $C_8SA$ , 10 mM EDC was added to 7.5 mM of  $C_{10}SA$ , and 1 mM of EDC (with 5 mM of NHS) was added to  $isoC_{10}$ . 15 minutes after the first batch of fuel, EDC was provided with a flux of 55 mM/h, 4 mM/h, 0.6 mM/h, and 0.05 mM/h, respectively, for  $C_6SA$ ,  $C_8SA$ ,  $C_{10}SA$ , and  $isoC_{10}$ . We added fuel by four batches per hour. The mixture was gently shaken after each addition.

### Analysis of the Kinetics of the Chemical Reaction Cycles

The concentration profiles of the chemical reaction networks were monitored over time by means of analytical HPLC. A 1.5 mL sample

was prepared as described above in a screw cap HPLC vial. The reaction solution was stored at  $25 \pm 1^\circ C$  solution, and samples of the solution were directly injected without further dilution. All reagents in the reaction cycle were separated using linear gradients of water and acetonitrile. See supporting information for more details.

**ESI.** ESI-MS measurements were performed using a Varian 500 MS LC ion trap spectrometer. The samples were diluted in acetonitrile and injected into an acetonitrile carrier flow (20  $\mu L/min$ ).

### Confocal Fluorescence Microscopy

Confocal fluorescence microscopy was performed on a Leica SP5 confocal microscope using a 63x oil immersion objective. Samples were prepared as described above but with 2.5  $\mu M$  Nile Red as a dye. 12–20  $\mu L$  of the sample was deposited on the PEG-coated glass slide and covered with a 12 mm coverslip. Every minute a  $4096 \times 4096$  pixel<sup>2</sup> image was acquired of an area that covered  $246 \mu m \times 246 \mu m$ . Each experiment was performed in triplicate ( $n = 3$ ). More details can be found in the Supporting Information.

### Image Analysis and Droplet Volume and Growth Rate Calculations

Images were analyzed with ImageJ's "analyze particles" package, from which we derived the volume of each droplet. We then calculated the average droplet volume per micrograph and binned several micrographs that were taken with one-minute intervals. The standard deviation was calculated between the three replicates of the experiments ( $n = 3$ ). From this dataset, the histograms of the droplet distributions were also calculated. We calculated the droplet growth by measuring the slope of the droplet volume over time for each individual experiment. Then, the average growth rate and the standard deviation between the three replicates were calculated ( $n = 3$ ). The droplet number was also obtained from the image analysis. Similar to the average droplet volume, the droplet number was obtained by binning all the image analysis droplet data in two-minute bins (for  $C_5$ ,  $C_6SA$ , and tBuPA) and five-minute bins (for  $C_6$ ,  $C_8SA$ ,  $C_{10}SA$ , and  $isoC_{10}$ ) to ensure a sufficient droplet number per unit of time. The standard deviation was calculated between 3 experiments ( $n = 3$ ).

### Theoretical Model and Classical Ostwald Ripening

Our reaction-diffusion model accounts for phase-separation and the fuel-driven chemical reactions. The underlying equations have been analyzed numerically and also used to find an explicit expression for the average volume as a function of the experimental parameters (e.g., solubility, surface tension, and diffusion constant). More information can be found in the SI. For our emulsions, we also calculated fusion rates and the Ostwald ripening rates based on theory from Lifshitz and Slyozov.<sup>[41]</sup>

### Author Contributions

J.B. and M.T.S. designed the experiments. J.J. and C.A.W. worked out the theory. M.T.S., C.W., F.S., H.P., B.R. J.M.G. carried out the experiments. J.B. and C.A.W. wrote the manuscript.

## Acknowledgments.

J.B. is grateful for funding by the Technical University of Munich – Institute for Advanced Study, funded by the German Excellence Initiative and the European Union Seventh Framework Programme under grant agreement n° 291763 and the European Research Council (ERC starting grant 852187). This research was conducted within the Max Planck School Matter to Life supported by the German Federal Ministry of Education and Research (BMBF) in collaboration with the Max Planck Society. H. P. and J. G. are grateful for funding by the Deutsche Forschungsgemeinschaft via the International Research Training Group ATUMS (IRTG 2022). M.T.S. acknowledges the European Union's Horizon 2020 Research and Innovation program for the Marie Skłodowska Curie Fellowship under grant agreement n° 747007. Financial support for C.W. comes from the Deutsche Forschungsgemeinschaft (DFG, German Research Foundation) – Project-ID 364653263 – TRR 235 Project 16. Open access funding enabled and organized by Projekt DEAL.

## Conflict of Interest

The authors declare no conflict of interest.

## Data Availability Statement

The data that support the findings of this study are available from the authors on reasonable request.

**Keywords:** active droplets · chemically fueled droplets · non-equilibrium self-assembly · phase separation · self-assembly

- [1] S. Alberti, *Curr. Biol.* **2017**, *27*, R1097–R1102.
- [2] S. F. Banani, H. O. Lee, A. A. Hyman, M. K. Rosen, *Nat. Rev. Mol. Cell Biol.* **2017**, *18*, 285–298.
- [3] W. Stroberg, S. Schnell, *Biophys. J.* **2018**, *115*, 3–8.
- [4] H. Zhang, S. Elbaum-Garfinkle, E. M. Langdon, N. Taylor, P. Occhipinti, A. A. Bridges, C. P. Brangwynne, A. S. Gladfelter, *Mol. Cell* **2015**, *60*, 220–230.
- [5] E. W. J. Wallace, J. L. Kear-Scott, E. V. Pilipenko, M. H. Schwartz, P. R. Laskowski, A. E. Rojek, C. D. Katanski, J. A. Riback, M. F. Dion, A. M. Franks, E. M. Airoidi, T. Pan, B. A. Budnik, D. A. Drummond, *Cell* **2015**, *162*, 1286–1298.
- [6] Y. Shin, C. P. Brangwynne, *Science* **2017**, *357*, eaaf4382.
- [7] S. Saha, C. A. Weber, M. Nusch, O. Adame-Arana, C. Hoegge, M. Y. Hein, E. Osborne-Nishimura, J. Mahamid, M. Jahnel, L. Jawerth, A. Pozniakovski, C. R. Eckmann, F. Jülicher, A. A. Hyman, *Cell* **2016**, *166*, 1572–1584.e16.
- [8] C. P. Brangwynne, C. R. Eckmann, D. S. Courson, A. Rybarska, C. Hoegge, J. Gharakhani, F. Jülicher, A. A. Hyman, *Science* **2009**, *324*, 1729–1732.
- [9] C. A. Weber, D. Zwicker, F. Jülicher, C. F. Lee, *Rep. Prog. Phys.* **2019**, *82*, 064601.

- [10] D. Zwicker, A. A. Hyman, F. Jülicher, *Phys. Rev. E* **2015**, *92*, DOI 10.1103/PhysRevE.92.012317.
- [11] J. D. Wurtz, C. F. Lee, *Phys. Rev. Lett.* **2018**, *120*, 078102.
- [12] C. A. Weber, C. F. Lee, F. Jülicher, *New J. Phys.* **2017**, *19*, 053021.
- [13] S. Krüger, C. A. Weber, J.-U. Sommer, F. Jülicher, *New J. Phys.* **2018**, *20*, 075009.
- [14] D. Zwicker, J. Baumgart, S. Redemann, T. Müller-Reichert, A. A. Hyman, F. Jülicher, *Phys. Rev. Lett.* **2018**, *121*, 158102.
- [15] D. Zwicker, R. Seyboldt, C. A. Weber, A. A. Hyman, F. Jülicher, *Nat. Phys.* **2017**, *13*, 408–413.
- [16] R. Seyboldt, F. Jülicher, *New J. Phys.* **2018**, *20*, 105010.
- [17] J. Leira-Iglesias, A. Sorrenti, A. Sato, P. A. Dunne, T. M. Hermans, *Chem. Commun.* **2016**, *52*, 9009–9012.
- [18] J. Boekhoven, A. M. Brizard, K. N. K. Kowligi, G. J. M. Koper, R. Eelkema, J. H. van Esch, *Angew. Chem. Int. Ed.* **2010**, *49*, 4825–4828; *Angew. Chem.* **2010**, *122*, 4935–4938.
- [19] J. Boekhoven, W. E. Hendriksen, G. J. M. Koper, R. Eelkema, J. H. van Esch, *Science* **2015**, *349*, 1075–1079.
- [20] K. Dai, J. R. Fores, C. Wanzke, B. Winkeljann, A. M. Bergmann, O. Lieleg, J. Boekhoven, *J. Am. Chem. Soc.* **2020**, *142*, 14142–14149.
- [21] S. Panja, B. Dietrich, D. J. Adams, *ChemSystemsChem* **2020**, *2*, e1900038.
- [22] S. P. Afrose, S. Bal, A. Chatterjee, K. Das, D. Das, *Angew. Chem. Int. Ed.* **2019**, *58*, 15783–15787.
- [23] A. Sorrenti, J. Leira-Iglesias, A. Sato, T. M. Hermans, *Nat. Commun.* **2017**, *8*, 15899.
- [24] W. A. Ogden, Z. Guan, *ChemSystemsChem* **2020**, *2*, e1900030.
- [25] S. Dhiman, R. Ghosh, S. J. George, *ChemSystemsChem* **2020**, *2*, e1900042.
- [26] S. Debnath, S. Roy, R. V. Ulijn, *J. Am. Chem. Soc.* **2013**, *135*, 16789–16792.
- [27] S. Maiti, I. Fortunati, C. Ferrante, P. Scrimin, L. J. Prins, *Nat. Chem.* **2016**, *8*, 725–731.
- [28] L. Heinen, A. Walther, *Sci. Adv.* **2019**, *5*, eaaw0590.
- [29] B. Rieß, C. Wanzke, M. Tena-Solsona, R. K. Grötsch, C. Maity, J. Boekhoven, *Soft Matter* **2018**, *14*, 4852–4859.
- [30] L. S. Kariyawasam, C. S. Hartley, *J. Am. Chem. Soc.* **2017**, *139*, 11949–11955.
- [31] R. K. Grötsch, A. Angi, Y. G. Mideksa, C. Wanzke, M. Tena-Solsona, M. J. Feige, B. Rieger, J. Boekhoven, *Angew. Chem. Int. Ed.* **2018**, *57*, 14608–14612.
- [32] R. K. Grötsch, C. Wanzke, M. Speckbacher, A. Angi, B. Rieger, J. Boekhoven, *J. Am. Chem. Soc.* **2019**, *141*, 9872–9878.
- [33] C. Wanzke, A. Jussupow, F. Kohler, H. Dietz, V. R. I. Kaila, J. Boekhoven, *ChemSystemsChem* **2020**, *2*, e1900044.
- [34] F. Schnitter, J. Boekhoven, *ChemSystemsChem*, **2020**, DOI: 10.1002/syst.202000037.
- [35] J. Leira-Iglesias, A. Tassoni, T. Adachi, M. Stich, T. M. Hermans, *Nat. Nanotechnol.* **2018**, *13*, 1021–1027.
- [36] M. Tena-Solsona, C. Wanzke, B. Riess, A. R. Bausch, J. Boekhoven, *Nat. Commun.* **2018**, *9*, 2044.
- [37] C. Donau, F. Späth, M. Sosson, B. Kriebisch, F. Schnitter, M. Tena-Solsona, H.-S. Kang, E. Salibi, M. Sattler, H. Mutschler, J. Boekhoven, *Nature Commun.* **2020**, 10.1038/s41467-020-18815-9.
- [38] M. Tena-Solsona, B. Rieß, R. K. Grötsch, F. C. Löhner, C. Wanzke, B. Käsdorf, A. R. Bausch, P. Müller-Buschbaum, O. Lieleg, J. Boekhoven, *Nat. Commun.* **2017**, *8*, 15895.
- [39] C. Wanzke, M. Tena-Solsona, B. Rieß, L. Lebcharani, J. Boekhoven, *Mater. Horiz.* **2020**, *7*, 1397–1403.
- [40] P. W. Voorhees, *Annu. Rev. Mat. Sci.* **1992**, *22*, 197–215.
- [41] I. M. Lifshitz, V. V. Slyozov, *J. Phys. Chem. Solids* **1961**, *19*, 35–50.
- [42] B. Alberts, *Mol. Biol. Cell*, Garland Science, Taylor And Francis Group, New York, NY, **2015**.

Manuscript received: July 3, 2020

Version of record online: October 15, 2020